

COMMUNICATION

[View Article Online](#)
[View Journal](#) | [View Issue](#)Cite this: *Nanoscale Adv.*, 2022, 4, 5021Received 17th August 2022
Accepted 3rd October 2022

DOI: 10.1039/d2na00549b

rsc.li/nanoscale-advances

Oxygen-evolving hollow polydopamine alleviates tumour hypoxia for enhancing photodynamic therapy in cancer treatment†

Qichen Zhan,^{‡*} Xuan Han,^{‡*} Jiankang Mu,^a Xianqing Shi,^c Yuhan Zheng,^a Ting Wang,^d Tao Cao,[‡] Yulu Xi,^a Zhongpei Weng,^g Xiaoqing Wang^g and Peng Cao^{*aef}

Hypoxia, a characteristic hallmark of solid tumours, restricts the therapeutic effect of photodynamic therapy (PDT) for cancer treatment. To address this issue, a facile and nanosized oxygen (O₂) bubble template is established by mixing oxygenated water and water-soluble solvents for guiding hollow polydopamine (HPDA) synthesis, and O₂ is encapsulated in the cavity of HPDA. HPDA with abundant catechol is designed as a carrier for zinc phthalocyanine (ZnPc, a boronic acid modified photosensitizer) via borate ester bonds to fabricate nanomedicine (denoted as HZNPs). The *in vitro* and *in vivo* results indicate that O₂-evolving HZNPs could alleviate tumour hypoxia and enhance PDT-anticancer efficiency. Melanin-like HPDA with a photothermal conversion rate (η) of 38.2% shows excellent synergistic photothermal therapy (PTT) efficiency in cancer treatment.

Introduction

Malignant cellular proliferation and vascular malformation lead to hypoxia formation in solid tumours.^{1,2} Insufficient oxygen (O₂) supply and consumption induce the invasion and metastasis of tumour cells.^{3,4} Hypoxia severely limits the

treatment outcome of O₂-medicated cancer therapies, especially photodynamic therapy (PDT).⁵

Great efforts have been made to alleviate tumour hypoxia for enhancing drug therapy efficiency, and these types can be divided into two categories, supplying exogenous O₂ to tumours (carrier or carrier-free) and catalysing endogenous hydrogen peroxide (H₂O₂) or H₂O to generate O₂.^{6–8} Delivering exogenous O₂ to alleviate tumour hypoxia is the most direct and effective method, and hyperbaric O₂ therapy increasing the pO₂ in the plasma and tumour tissues has been used in clinical PDT for cancer treatment.⁹ In recent years, haemoglobin (Hb), liposomes and macrovesicle materials were designed as carriers for O₂ delivery. Hb, an iron-rich metalloprotein in red blood cells composed of globin and heme, could highly bind and deliver O₂ in intravenous transmission.¹⁰ However, free Hb is susceptible to auto-oxidation during circulation and results in renal toxicity and cardiovascular complications.¹¹ Liposomes embedded with microbubbles have been approved by the FDA as an ultrasound contrast agent for echocardiography.¹² Its disadvantage is that the O₂ loading efficiency is approximately 10% by volume, indicating that it is sufficient for delivering potent bioactive gases, such as NO and Xe, but not suitable for O₂.¹³ Compared with liposomes, hollow materials have a core and a high loading efficiency for O₂. How to fabricate a satisfactory O₂ carrier to alleviate tumour hypoxia is still a big challenge.

Polydopamine (PDA) is an ideal carrier for drug delivery because of its good biocompatibility.¹⁴ PDA formation shares many common characteristics with the melanin synthetic pathway, and its photothermal conversion rate (η) could reach up to 40%.¹⁵ Under alkaline conditions, dopamine (DA) monomers were oxidized to DA quinone and a five-membered ring, then rearranged to 5,6-dihydroxyindoles and aggregated with other polymers.¹⁶ More importantly, the polymerization rate of DA at the gas–liquid interface is higher than that in the solutions,^{17,18} indicating that the O₂ bubble template may guide PDA polymerization. Chen's group reported a method for O₂-rich PDA microcapsule preparation in 2021, but the micron-sized aggregates limited its further application in cancer treatment.¹⁹

^aSchool of Pharmacy, Nanjing University of Chinese Medicine, Nanjing, Jiangsu, 210023, China. E-mail: zhanqichen@njucm.edu.cn; cao_peng@njucm.edu.cn

^bSchool of Chinese Medicine, Nanjing University of Chinese Medicine, Nanjing, Jiangsu, 210023, China

^cDepartment of Public Experimental Teaching, Nanjing University of Aeronautics and Astronautics, Nanjing, Jiangsu, 211106, China

^dInstitute of Chemical Industry of Forest Products, Chinese Academy of Forestry, Nanjing, Jiangsu, 210042, China

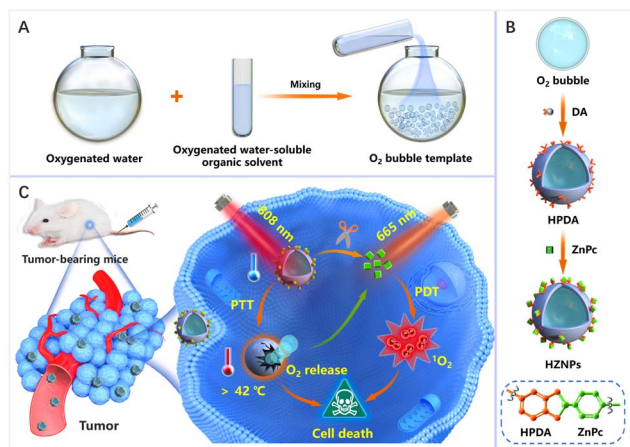
^eAffiliated Hospital of Integrated Traditional Chinese and Western Medicine, Nanjing University of Chinese Medicine, Nanjing, Jiangsu, 210028, China

^fZhenjiang Hospital of Chinese Traditional and Western Medicine, Zhenjiang, Jiangsu, 212002, China

^gGaoyou Hospital of Traditional Chinese Medicine, Yangzhou, Jiangsu, 225600, China

† Electronic supplementary information (ESI) available. See DOI: <https://doi.org/10.1039/d2na00549b>

‡ Q. C. Zhan and X. Han contributed equally to this work.



Scheme 1 (A) Schematic diagram of O₂ bubble formation by mixing oxygenated water and water-soluble organic solvents. (B) HZNP fabrication and (C) the mechanism of HZNPs alleviating tumour hypoxia to enhance PDT efficiency.

As shown in Scheme 1, a facile and nanosized O₂ bubble template is reported by mixing oxygenated water and oxygenated water-soluble organic solvents. The O₂ bubble template guided DA polymerization to form hollow PDA (HPDA) and encapsulate O₂ simultaneously. Furthermore, HPDA is designed as a carrier for zinc phthalocyanine (ZnPc) to fabricate pH-responsive nanomedicine (denoted HZNPs). The ZnPc release rate of HZNPs reached 64.9% in a simulated tumour microenvironment. The *in vitro* and *in vivo* results indicated that HZNPs could deliver O₂ to alleviate tumour hypoxia, inhibit the expression of hypoxia-induced factor-1 (HIF-1 α), and enhance the anticancer efficiency of PDT. Upon the combination of light irradiation (808 nm + 665 nm), HZNP treated groups achieved satisfactory outcomes by PTT and PDT.

Results and discussion

Gas solubility in solvents is closely related to polarity, and mixing different solvents could change gas solubility, such as water and water-soluble organic solvents.^{20–22} Polarity difference changes resulted in gas accumulation which escapes in the form of bubbles.²³ To obtain nanosized O₂ bubbles, the air (mainly N₂ and O₂) dissolved in water and water-soluble organic solvents was removed using a vacuum pump. These solvents were replenished with O₂ to form O₂-rich solutions respectively.

After mixing oxygenated water and four water-soluble alcohols respectively, O₂ solubility in these mixtures was monitored using an O₂ dissolving meter. The results revealed that O₂ solubility decreased and the biggest change was the mixture of *n*-propanol and water (Fig. 1A–D). The excess O₂ escaped from methanol/water, ethanol/water, isopropanol/water, and *n*-propanol/water was 3.71 mL L^{−1}, 5.46 mL L^{−1}, 4.97 mL L^{−1} and 7.14 mL L^{−1}, respectively. We further studied the size and morphology of O₂ bubbles by taking *n*-propanol/water as an instance at different time points. As shown in Fig. 1E, the dynamic light scattering (DLS) distribution showed that the

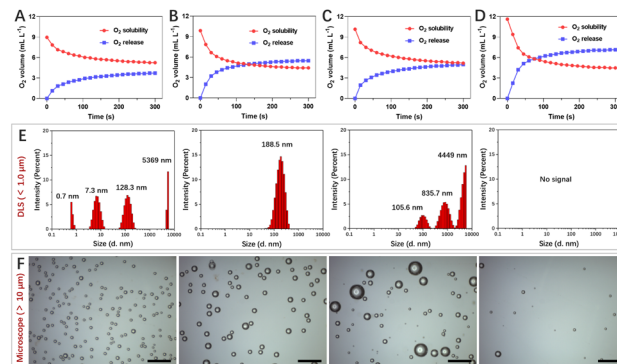


Fig. 1 The O₂ solubility and O₂ release behaviours in four types of oxygenated alcohols and water mixtures (A, methanol/water; B, ethanol/water; C, isopropanol/water; D, *n*-propanol/water). (E) The DLS distribution and (F) the corresponding morphology images of O₂ bubbles in the mixture of oxygenated *n*-propanol and water at different time points (2 min; 10 min; 20 min and 60 min; bar = 50 μm).

sizes of O₂ bubbles were uneven, ranging from 0.7 nm to 5369 nm. These small O₂ bubbles were fragile and fused with other bubbles to form larger bubbles. Interestingly, these O₂ bubbles with an average size of 188.5 nm remained in existence stably for 10 min. Their generation, fusion and escape processes were also confirmed using a microscope (Fig. 1F).

The polymerization rate of DA monomers at the gas–liquid interface is two times faster than that in solution.¹⁷ Therefore, we speculated that O₂ bubbles are promising as a template for guiding DA polymerization to fabricate HPDA. To prove this hypothesis, after mixing oxygenated water and oxygenated *n*-propanol, DA monomers were added to the mixing solution. The PDA formation process was monitored using a transmission electron microscope (TEM). As shown in Fig. 2A, DA cyclization and covalent cross-linking to form composite films at the gas–liquid interface occur. The Raman spectra confirmed that HPDA was similar to eumelanin (Fig. S1†). Compared with PDA nanobowls, HPDA would not break with the increasing pressure inside the O₂ bubbles.²³ However, after removing the O₂ bubble template, DA polymerized to form PDA nanospheres (Fig. S2†). We further utilized the O₂ bubble template generated by mixing other oxygenated water-soluble organic solvents (methanol, alcohol, and isopropanol) with oxygenated water to prepare HPDA successfully (Fig. S3†), indicating the general applicability of the O₂ bubble template for guiding PDA polymerization. The shell thickness of HPDA could be easily controlled by adjusting the reaction time (Fig. S4†).

Furthermore, HPDA was designed as a carrier for ZnPc *via* boric acid ester to fabricate HZNPs. As shown in Fig. 2B and C, HZNPs were observed by using TEM and a scanning electron microscope (SEM), and HZNPs presented regular hollow structures with an average size of 156.1 nm (Fig. 2E). The elemental mapping patterns of HZNPs showed that C, N and O were derived from HPDA and ZnPc while Zn was derived from ZnPc, confirming the successful preparation of HZNPs (Fig. 2D). In addition, HZNPs showed UV-vis absorption in the B-band (200–300 nm) and Q-band (600–800 nm), which was attributed to the



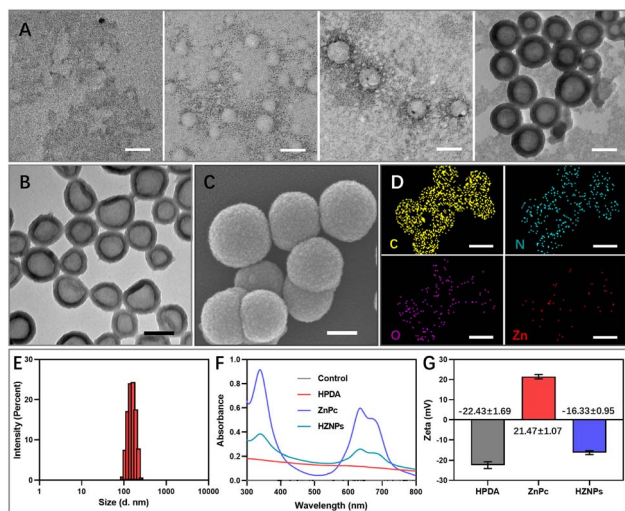


Fig. 2 (A) The TEM images of HPDA formation at different time points (0 min; 5 min; 10 min; 45 min) in *n*-propanol/water solution. (B) TEM and (C) SEM images of HZNPs (the SEM sample of HZNPs was sprayed with platinum powder two times). (D) The elemental mapping analysis of HZNPs. (E) The DLS distribution of HZNPs in distilled water. (F) The UV-vis absorbance of HPDA, ZnPC and HZNPs in distilled water. (G) The zeta potential comparison of HPDA, ZnPC and HZNPs in distilled water (all bars are 100 nm).

characteristic π - π^* electron transition of ZnPC.²⁴ The broad-spectrum absorption ability of HPDA resulted in the increasing absorbance of HZNPs (Fig. 2F). As shown in Fig. 2G, ZnPC loading in HZNPs also increased the zeta potential of HZNPs. The inductively coupled plasma spectrometer (ICP) data indicated that the average loading efficiency of ZnPC in HZNPs was 0.2891 mg mg⁻¹ (Table S1†). To further study the stability of HZNPs, the DLS distribution of HZNPs was detected in PBS and the cell culture medium. As shown in the DLS results, no obvious HZNP aggregation was detected in PBS or DMEM+10% bovine serum, indicating its good stability in these bio-surroundings (Fig. S5†).

HPDA with abundant catechol could form borate ester bonds with ZnPC, and the pH-responsive borate ester bond was broken under acidic conditions.²⁵ The vigorous metabolism and profound hypoxia in tumour tissue led to cell glycolysis and superfluous acid substance generation.^{26,27} Then, pH-triggered ZnPC release behaviours of HZNPs were studied under acidic conditions. As shown in Fig. 3A and S6,† the release rate of ZnPC from HZNPs increased obviously under acidic conditions while a slight change was observed under normal conditions, and the ZnPC release rate reached 64.9% when the pH is 5.5, which will recover PDT-mediated antitumor activity (Fig. 3A, S6 and S7†).

Even though HPDA has good stability due to its extensive covalent and noncovalent interactions, HPDA could be degraded in H₂O₂ aqueous solution because the -OH group in HPDA was oxidized to C=O and -COOH groups (Fig. S8†). To study the encapsulation ability of HZNPs for O₂, the Ru(dpp)₃-Cl₂, a commercial O₂-quenching fluorescence probe, was used to detect the O₂ levels of different samples. As shown in Fig. 3B and S9,† the fluorescence intensity of the HPDA and HZNP

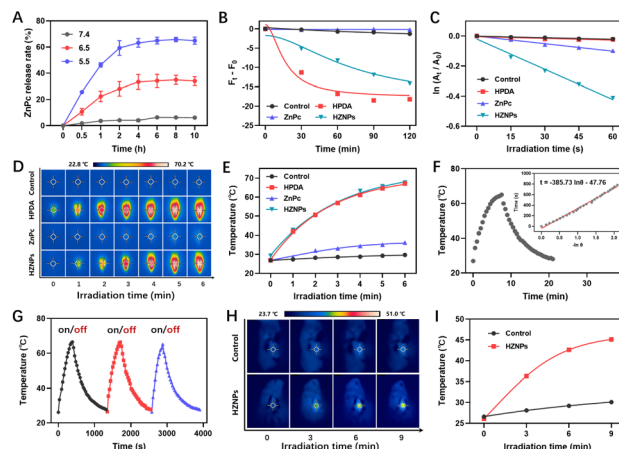


Fig. 3 (A) Time-dependent release behaviours of ZnPC from HZNPs in solution with pH ranging from 5.5 to 7.4. (B) O₂ level in enclosed and hypoxic aqueous solution treated with different drugs (HPDA, ZnPC and HZNPs) was measured using Ru(dpp)₃Cl₂ (H₂O₂, 200 μ M). (C) The ¹O₂ generation ability of different drugs was detected using ADPA under hypoxic conditions (665 nm, LED, 0.45 W cm⁻²). (D) The photothermal images and (E) temperature change of different drugs under light irradiation (808 nm, laser, 1.0 W cm⁻²). (F) The cooling temperature curve of HPDA in distilled water with turn on/off laser irradiation, and the cooling time (*t*) curve versus the negative natural logarithm of the temperature driving force ($-\ln \theta$). (G) Three photothermal conversion cycles of HPDA. (H) The photothermal images of tumour-bearing mice under laser irradiation and (I) the corresponding temperature change curve (808 nm, laser, 0.3 W cm⁻²).

treated groups decreased obviously while the ZnPC treated group showed a slight change, indicating that HPDA and HZNPs could increase the O₂ level under hypoxic conditions. We further investigated the effect of HPDA-mediated PTT on the stability of HZNPs. After being dispersed in H₂O₂ aqueous solution for 30 min, HZNPs decomposed slightly at room temperature (Fig. S10†). In contrast, after laser irradiation for 30 min, HZNPs decomposed rapidly, revealing that PTT may promote the O₂ release and alleviate tumour hypoxia. Singlet oxygen (¹O₂), a pivotal evaluation indicator for the photosensitizer, is positively related to the O₂ level.²⁸ After light irradiation, the ¹O₂ generation ability of different drugs was evaluated using 3,3'-(anthracene-9,10-diyl)dipropionic acid (ADPA). As can be seen from Fig. 3C and S11,† the ADPA absorbance bleaching at 378 nm showed that the order of ¹O₂ generation efficiency of different drugs was $k_{\text{HZNPs}} (6.71 \times 10^{-3}) > k_{\text{ZnPC}} (1.67 \times 10^{-3}) > k_{\text{HPDA}} (0.39 \times 10^{-3}) > k_{\text{Control}} (0.34 \times 10^{-3})$, indicating that the high ¹O₂ generation efficiency of HZNPs was attributed to ZnPC and the increasing O₂ level.

Melanin-like PDA has strong photothermal properties,²⁹ and the photothermal conversion rate (η) of HZNPs was measured with a photothermal imager. After laser irradiation for 5 min, the temperature of HPDA and HZNP solutions reached up to 67.1 °C and 67.6 °C respectively, while that of ZnPC was 36.2 °C, revealing that the η of HZNPs was mainly derived from HPDA (Fig. 3D and E). To calculate the η of HPDA, the absorbance of HPDA was detected to be 0.3073 at 808 nm (Fig. S12†). The temperature of HPDA solution raised to the highest upon laser



irradiation, then, the laser was turned off, and the natural cooling temperature of HPDA solution was recorded at different points of time. The cooling time (t) curve *versus* the negative natural logarithm of temperature driving force ($-\ln \theta$) is shown in Fig. 3F. The time constant (τ) for heat transfer in the system was calculated to be 385.73 and the η was determined to be 38.2%. Three photothermal cycles showed that photothermal conversion capacity decreased slightly, indicating that HPDA has good stability (Fig. 3G). Furthermore, the photothermal properties of HZNPs were measured in tumour-bearing mice. After laser irradiation for 9 min, the temperature of the right solid tumour reached up to 45.1 °C, suggesting that HZNPs could kill tumour cells by PTT (Fig. 3H and I).

HZNP alleviating hypoxia behaviour *in vitro* was detected using $\text{Ru}(\text{dpp})_3\text{Cl}_2$ under hypoxic conditions.³⁰ Compared with others, the fluorescence intensity of the ZnPc treated group increased obviously upon light irradiation because of PDT-depletion of O_2 . However, even though PDT consumed O_2 , the HZNP treated group still showed no fluorescence change, which indicated that O_2 released from HZNPs alleviated intracellular hypoxia (Fig. 4A and B). O_2 is an important component in PDT since the light initiated $^1\text{O}_2$ generated by photosensitizers needs O_2 motivation.³⁰ Therefore, we speculated that O_2 -evolving HZNPs could enhance the anticancer activity of PDT. To verify this speculation, Singlet Oxygen Sensor Green (SOSG) was used to measure the intracellular $^1\text{O}_2$ generation ability of different drugs. Under hypoxic conditions, the HPDA and ZnPc treated groups all showed weak fluorescence while the HZNP treated group showed fluorescence enhancement upon light irradiation (Fig. 4C and D). All these results above indicated that HZNPs released O_2 and improved the generation ability of ZnPc in tumour cells.

To further elucidate drugs' anticancer mechanisms, the intracellular localization of ZnPc and HZNPs was measured using a confocal laser scanning microscope. As shown in Fig. 4E, the colocalization overlap of drugs and probes (Mito-Tracker Green or Lyso-Tracker Blue) suggested that the action site of HZNPs was the lysosome. Cell Counting Kit-8 (CCK8) assay was used to detect drugs' dark toxicity and phototoxicity under normoxic and hypoxic conditions. First of all, we tested the IC_{50} value of each formulation. The IC_{50} values of light treated groups were remarkably lower than those of non-light treated groups, indicating that light was one crucial factor in damaging tumour cells (Table S2†). Furthermore, all drugs showed no cytotoxicity without light irradiation (Fig. 4F). After different light irradiations, the HPDA treated group and ZnPc treated group showed PTT-induced (808 nm) and PDT-induced (665 nm) 4T1 cell growth inhibition effects, respectively. The HZNPs have combined and more efficient PTT and PDT anticancer effects under normoxic conditions (Fig. 4G). In contrast, the PDT-induced cell death rate by ZnPc decreased obviously under hypoxic conditions, and the anticancer efficiency of HZNPs was superior to that of ZnPc, indicating that HZNPs could alleviate tumour hypoxia (Fig. 4H).

The phototoxicity of different drugs *in vivo* was studied in tumour-bearing mice by monitoring the tumour volume change during 14 days of treatment. The metabolism distribution of

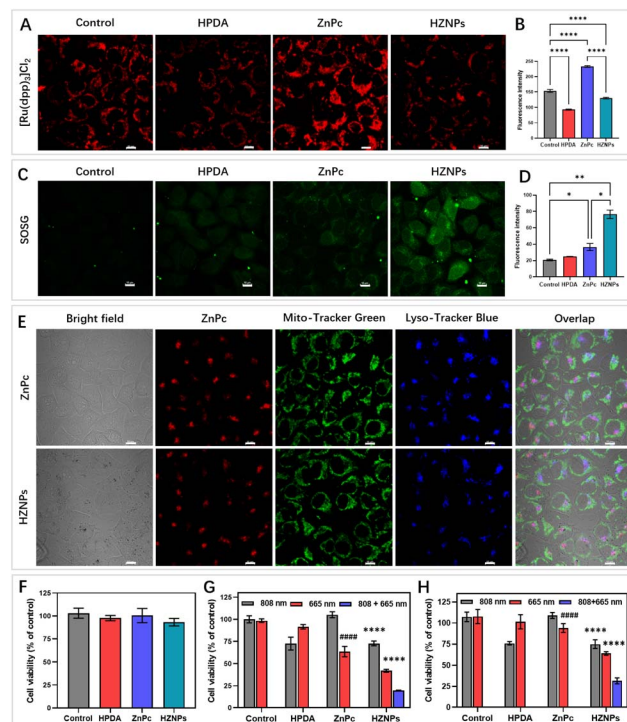


Fig. 4 (A) Intracellular O_2 of the drug (HPDA, ZnPc and HZNPs) treated group was detected using $\text{Ru}(\text{dpp})_3\text{Cl}_2$ and (B) the comparative fluorescence intensity under hypoxic conditions ($****P < 0.0001$). (C) Intracellular $^1\text{O}_2$ of different drugs was detected using the SOSG probe and (D) the comparative fluorescence intensity under hypoxic conditions ($**P < 0.01$; $*P < 0.05$). (E) The laser scanning confocal images of drugs (ZnPc or HZNPs) and the subcellular organelles probe (Mito-Tracker Green or Lyso-Tracker Blue) in tumour cells. (F) The cell cytotoxicity evaluation of various drugs using CCK8 assay. The cell phototoxicity of various drugs treated with different light sources under (G) normoxic conditions ($****P < 0.0001$ HZNPs treated with 808 nm and HZNPs treated with 665 nm versus HZNPs treated with 808 nm + 665 nm; $****P < 0.0001$ ZnPc treated with 665 nm versus HZNPs treated with 665 nm versus HZNPs treated with 808 nm and HZNPs treated with 665 nm) and (H) hypoxic conditions ($****P < 0.0001$ HZNPs treated with 808 nm and HZNPs treated with 665 nm versus HZNPs treated with 808 + 665 nm; $****P < 0.0001$ ZnPc treated with 665 nm versus HZNPs treated with 665 nm). (All bars are 10 μm ; 808 nm, laser, 0.3 W cm^{-2} ; 665 nm, LED, and 0.45 W cm^{-2}).

ZnPc and HZNPs in mice was monitored using an IVIS Lumina LT system. Compared with the ZnPc treated group, the stronger fluorescence intensity of the HZNP treated group suggested that HZNPs have a better retention effect in solid tumours (Fig. 5A, B and S13†). In addition, the relative amount of the Zn element in the main organs and tumours of tumour-bearing mice was measured by inductively coupled plasma mass spectrometry (ICP-MS). The relative amount of the Zn element in tumours treated with HZNPs was 8.16 mg g^{-1} , 2.6 times that of the ZnPc treated group (3.15 mg g^{-1}). Compared with the ZnPc treated group, HZNPs accumulated in the kidney decreased, which was beneficial to reduce the side effects of ZnPc (Table S3†). Many literature studies reported that nanomedicine accumulated in tumour and inflamed tissue by the enhanced EPR effect.^{31,32} Recent scientific studies indicated the passive accumulation of nanomedicines at the tumour site is not as important as the



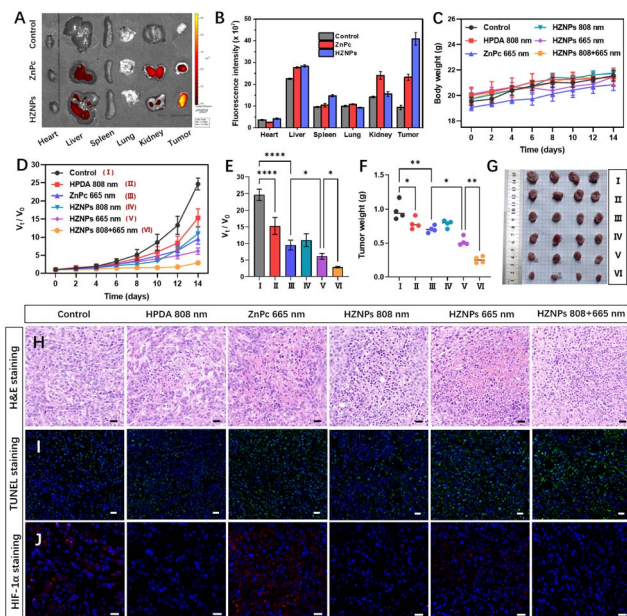


Fig. 5 (A) The metabolism distribution of ZnPc and HZNPs in main organs and tumours and (B) the comparative fluorescence intensity. (C) The body weight change of mice treated with different drugs during 14 days of treatment. (D) The relative tumour volume (V/V_0) change of tumour-bearing mice during 14 days of treatment and (E) the comparison of significant differences using a one-way ANOVA (I, Control; II, HPDA + 808 nm; III, ZnPc + 665 nm; IV, HZNPs + 808 nm; V, HZNPs + 665 nm; VI, HZNPs + 808 nm + 665 nm; 808 nm, laser, 0.3 W cm^{-2} ; 665 nm, laser, 0.32 W cm^{-2}). (F) The tumour weight and (G) image of tumour-bearing mice treated with different drugs after 14 days of treatment. (H) H&E staining and (I) TUNEL staining of tumour slides sacrificed from tumour-bearing mice after 14 days of treatment. (J) The immunofluorescence staining of tumour slides treated with HIF-1 α antibodies (Blue, DAPI; Red, HIF-1 α antibody; All bars are 20 μm).

proposed classical EPR effect because of few gaps along tumour blood vessels.³³ Therefore, the trans endothelial pathway and EPR effect may both contribute to the high accumulation of HZNPs at tumour sites.

There was no body weight decrease in mice in our study (Fig. 5C). The haematoxylin and eosin (H&E) stained tissue slices of main organs dissected from sacrificial mice showed no pathological features (Fig. S14†). The tumour growth inhibition of different drugs was studied by tumour volume tracking and H&E staining. HPDA treated with 808 nm light and ZnPc treated with 665 nm light showed tumour growth suppression to some extent *via* PTT (19.18%) and PDT (27.88%), respectively. The anticancer efficiency (46.29%) of HZNPs + 665 nm was superior to that (27.88%) of ZnPc + 665 nm, which could be ascribed to the hypoxia alleviating ability of HZNPs at tumour sites. The synergetic PTT and PDT of HZNPs achieved the best anticancer efficiency (73.91%, Fig. 5D–G). H&E staining of pathological tumour slices showed the most serious nuclei damage (purple blue, stained with haematoxylin) occurred in the group of HZNPs treated with 808 nm plus 665 nm light irradiation (Fig. 5H). After treatment with different formulations, the cell apoptosis in the excised tumour tissues was studied by means of

TUNEL. As shown in Fig. 5I, the cell apoptosis of the HZNPs + 665 nm treated group was higher than that of the ZnPc + 665 nm treated group, and HZNPs treated with combination light (808 nm + 665 nm) had the best anticancer efficiency, which was consistent with the results of H&E staining. Furthermore, the hypoxia-inducible factor (HIF)-1 α staining assay was used to evaluate the hypoxic condition in the tumours of different groups. The tumour immunofluorescence of ZnPc treated with 665 nm light was stronger than that of control, implying that the O_2 -depletion of PDT resulted in HIF-1 α overexpression. Even if the PDT process consumed O_2 in tumours, the immunofluorescence intensity was still weak in the HZNP treated group, indicating that the HIF-1 α expression was inhibited by the O_2 -evolving HZNPs (Fig. 5J).

Conclusions

In conclusion, a facile and nanosized O_2 bubble template was reported by mixing oxygenated water and water-soluble organic solvents. O_2 -evolving HPDA was prepared based on the nanosized O_2 bubble template, which would inspire the gas bubble template for guiding materials synthesis. The *in vitro* and *in vivo* results revealed that HZNPs could release O_2 and alleviate hypoxia to enhance the PDT efficiency. Under a combination of light (808 nm + 665 nm) irradiation, HZNPs achieved synergetic and satisfactory anticancer efficiency, and the tumour growth rate was suppressed up to 73.91% when compared to that of control mice. Our study provides a novel strategy for O_2 delivery by nanomaterials in cancer treatment.

Conflicts of interest

There are no conflicts to declare.

Acknowledgements

This research was financially supported by the National Natural Science Foundation of China (grant no. 82104686; 82125037) and Nanjing University of Chinese Medicine (XPT82104686).

Notes and references

- 1 C. Zhang, W. J. Qin, X. F. Bai and X. Zhang, *Nano Today*, 2020, **35**, 100960.
- 2 X. Li, K. Kwon, T. Guo, Z. Liu and J. Yoon, *Angew. Chem., Int. Ed.*, 2018, **57**, 11522.
- 3 W. Meng, Y. Hao, C. He and G. Zhu, *Mol. Cancer*, 2019, **18**, 1–14.
- 4 E. L. LaGory and A. J. Giaccia, *Nat. Cell Biol.*, 2016, **18**, 356.
- 5 X. Liang, M. Chen, P. Bhattacharai, S. Hameed and Z. Dai, *ACS Nano*, 2020, **14**, 13569.
- 6 Y. Wan, L. H. Fu, C. Li, J. Lin and P. J. Huang, *Adv. Mater.*, 2021, **33**, 2103978.
- 7 Y. Cheng, H. Cheng, C. Jiang, X. Qiu, K. Wang, W. Huan, A. Yuan, J. Wu and Y. Q. Hu, *Nat. Commun.*, 2015, **6**, 8785.
- 8 R. Li, C. Zhang, B. Xie, W. Yu, W. Qiu, H. Cheng and X. Zhang, *Biomaterials*, 2019, **194**, 84.



- 9 I. Moen and L. E. Stuhr, *Target. Oncol.*, 2012, **7**, 233.
- 10 H. Wang, J. Li, Y. Wang, X. Gong, X. Xu, J. Wang, Y. Li, X. Sha and Z. Zhang, *J. Control. Release*, 2020, **319**, 25.
- 11 T. Li, X. Jing and Y. Huang, *Macromol. Biosci.*, 2011, **11**, 865.
- 12 S. M. Fix, M. A. Borden and P. A. Dayton, *J. Control. Release*, 2015, **209**, 139.
- 13 S. Huang, D. D. McPherson and R. C. MacDonald, *Ultrasound Med. Biol.*, 2008, **34**, 1272.
- 14 Y. Liu, K. Ai and L. Lu, *Chem. Rev.*, 2014, **114**, 5057.
- 15 Q. Zhan, X. Shi, J. Zhou, L. Zhou and S. Wei, *Small*, 2019, **15**, 1803926.
- 16 N. F. Della Vecchia, R. Avolio, M. Alfè, M. E. Errico, A. Napolitano and M. d'Ischia, *Adv. Funct. Mater.*, 2013, **23**, 1331.
- 17 F. Ponzio, P. Payammar, A. Schneider, M. Winterhalter, J. Bour, F. Addiego, M. P. Krafft, J. Hemmerle and V. Ball, *J. Phys. Chem. Lett.*, 2014, **5**, 3436.
- 18 H. Yang, Q. Wu, L. Wan and Z. Xu, *Chem. Commun.*, 2013, **49**, 10522.
- 19 B. Wu, Z. Sun, J. Wu, J. Ruan, P. Zhao, K. Liu, C. Zhao, J. Sheng, T. Liang and D. Chen, *Angew. Chem., Int. Ed.*, 2021, **60**, 9284.
- 20 S. Yang, S. M. Dammer, N. Bremond, H. J. Zandvliet, E. S. Kooij and D. J. Lohse, *Langmuir*, 2007, **23**, 7072.
- 21 S. Karpitschka, E. Dietrich, J. R. Seddon, H. J. Zandvliet, D. Lohse and H. J. Riegler, *Phys. Rev. Lett.*, 2012, **109**, 066102.
- 22 L. A. Palmer, D. Cookson and R. N. Lamb, *Langmuir*, 2011, **27**, 144.
- 23 Q. Zhan, X. Shi, D. Fan, L. Zhou and S. Wei, *Chem. Eng. J.*, 2021, **404**, 126443.
- 24 A. Ogunsipe, D. Maree and T. J. Nyokong, *J. Mol. Struct.*, 2003, **650**, 131.
- 25 R. Liu, Y. Guo, G. Odusote, F. Qu and R. D. Priestley, *ACS Appl. Mater. Interfaces*, 2013, **5**, 9167.
- 26 V. Estrella, T. Chen, M. Lloyd, J. Wojtkowiak, H. H. Cornnell, A. Ibrahim-Hashim, K. Bailey, Y. Balagurunathan, J. M. Rothberg, B. F. Sloane, J. Johnson, R. A. Gatenby and R. J. Gillies, *Cancer Res.*, 2013, **73**, 1524.
- 27 R. A. Cardone, V. Casavola and S. J. Reshkin, *Nat. Rev. Cancer*, 2005, **5**, 786.
- 28 H. Zhao, J. Xu, Y. Wang, C. Sun, L. Bao, Y. Zhao, X. Yang and Y. Zhao, *ACS Nano*, 2022, **16**, 3070.
- 29 X. Zeng, M. Luo, G. Liu, X. Wang, W. Tao, Y. Lin, X. Ji, L. Nie and L. Mei, *Adv. Sci.*, 2018, **5**, 1800510.
- 30 H. Chen, J. Tian, W. He and Z. Guo, *J. Am. Chem. Soc.*, 2015, **137**, 1539.
- 31 H. Maeda, H. Nakamura and J. Fang, *Adv. Drug Delivery Rev.*, 2013, **65**, 71.
- 32 H. Kang, S. Rho, W. R. Stiles, S. Hu, Y. Baek, D. W. Hwang, S. Kashiwagi, M. S. Kim and H. S. Choi, *Adv. Healthcare Mater.*, 2020, **9**, 1901223.
- 33 S. Sindhwani, A. M. Syed, J. Ngai, B. R. Kingston, L. Maiorino, J. Rothschild, P. MacMillan, Y. Zhang, N. U. Rajesh, T. Hoang, J. Wu, S. Wilhelm, A. Zilman, S. Gadde, A. Sulaiman, B. Ouyang, Z. Lin, L. Wang, M. Egeblad and W. Chan, *Nat. Mater.*, 2020, **19**, 566.

